JBC RESEARCH ARTICLE

Structural variations between small alarmone hydrolase dimers support different modes of regulation of the stringent response

Received for publication, April 27, 2022, and in revised form, June 10, 2022 Published, Papers in Press, June 15, 2022,
https://doi.org/10.1016/j.jbc.2022.102142

Francesco Bisiak[1], Adriana Chrenková[1], Sheng-Da Zhang[2], Jannik N. Pedersen[3], Daniel E. Otzen[1,3], Yong E. Zhang[4], and Ditlev E. Brodersen[1,*]

From the [1]Department of Molecular Biology and Genetics, Aarhus University, Aarhus C, Denmark; [2]Department of Biotechnology and Biomedicine, Technical University of Denmark, Kgs. Lyngby, Denmark; [3]Interdisciplinary Nanoscience Centre (iNano), Aarhus University, Aarhus C, Denmark; [4]Department of Biology, University of Copenhagen, København N, Denmark

Edited by Ursula Jakob

The bacterial stringent response involves wide-ranging metabolic reprogramming aimed at increasing long-term survivability during stress conditions. One of the hallmarks of the stringent response is the production of a set of modified nucleotides, known as alarmones, which affect a multitude of cellular pathways in diverse ways. Production and degradation of these molecules depend on the activity of enzymes from the RelA/SpoT homologous family, which come in both bifunctional (containing domains to both synthesize and hydrolyze alarmones) and monofunctional (consisting of only synthetase or hydrolase domain) variants, of which the structure, activity, and regulation of the bifunctional RelA/SpoT homologs have been studied most intensely. Despite playing an important role in guanosine nucleotide homeostasis in particular, mechanisms of regulation of the small alarmone hydrolases (SAHs) are still rather unclear. Here, we present crystal structures of SAH enzymes from *Corynebacterium glutamicum* ($RelH_{Cg}$) and *Leptospira levettii* ($RelH_{Ll}$) and show that while being highly similar, structural differences in substrate access and dimer conformations might be important for regulating their activity. We propose that a varied dimer form is a general property of the SAH family, based on current structural information as well as prediction models for this class of enzymes. Finally, subtle structural variations between monofunctional and bifunctional enzymes point to how these different classes of enzymes are regulated.

The stringent response is a fundamental mechanism for bacterial survival (1) necessary to cope with metabolic and oxidative stress (2–6), to increase survival during infection (7, 8) and for the development of drug tolerance and resistance (9–11). This is achieved through the inhibition of transcription of genes involved in bacterial growth (12) as well as suppression of DNA replication and protein as well as nucleotide synthesis in preparation for long term survival (1, 4, 13, 14). The signal molecules mainly responsible for triggering the stringent response are guanosine 3′-diphosphate 5′-triphosphate (pppGpp) and guanosine 3′,5′-bis(diphosphate) (ppGpp) (15, 16). In addition, guanosine 3′-diphosphate 5′-monophosphate (pGpp) was recently shown to also contribute to the stringent response in some bacteria, such as *Enterococcus faecalis* and *Bacillus subtilis* (17–19). Collectively, these molecules are referred to as alarmones or (pp)pGpp. Alarmones are synthesized by transfer of the β and γ phosphates of ATP to the 3′-hydroxyl group of GTP, GDP, or GMP by the synthetase domain of enzymes belonging to the RelA-SpoT homologous (RSH) superfamily (13, 20), generating pppGpp, ppGpp, or pGpp, respectively (21, 22). Subsequent removal of these signal molecules, which is critical for cellular (pp)pGpp homeostasis, is achieved in a pyrophosphohydrolase reaction in which the δ and ε phosphate groups are released in the form of pyrophosphate and the original nucleotide is regenerated (23–25).

The (pp)pGpp hydrolase activity is maintained by enzymes containing a metal-dependent hydrolase (HD) domain (24), which is well conserved within the RSH family of bi-functional synthetases/hydrolases (20). These are so-called "long" bifunctional enzymes that contain both a synthetase and hydrolase domain in addition to several C-terminal regulatory domains required for controlling the activity of the two catalytic domains (20). In these enzymes, the predominant activity (synthetase/hydrolase) is controlled through a combination of external and internal inputs such as ribosome binding (26–28), the state of the regulatory domains (27, 29, 30), and allosteric interaction between the synthetase and hydrolase site (23, 31) ensuring that either synthesis or hydrolysis predominates at any given time. In addition to the bifunctional RSHs, many bacterial species encode monofunctional variants known as small alarmone hydrolases (SAHs) and small alarmone synthetases (SASs) that lack any regulatory domains (20). While long RSHs have been extensively studied (1, 32–36), much less is known about the regulation of the monofunctional variants although they appear to be regulated through higher-order oligomeric structure. For example, the *B. subtilis* (p)ppGpp SAS RelQ is regulated through alarmone binding at an allosteric site inside a higher-order, tetrameric enzyme (37). Moreover, pervasive searches for homologs of these enzymes have revealed intriguing new

* For correspondence: Ditlev E. Brodersen, deb@mbg.au.dk.

regulatory principles, such as the ability of toxic SAS and some SAHs to act as toxin-antitoxin systems (38, 39).

SAHs contain a well-conserved HD domain (24) for which information was derived by comparison to the corresponding domain of long RSHs (23, 26–28, 31, 40, 41). The exact catalytic mechanism as well as mode of regulation of the SAH enzymes, however, have not yet been described in detail. Generally, six conserved catalytic residues, or motifs (HD1-HD6), are involved in the Mn^{2+}-dependent reaction (23, 25, 42, 43). HD1 and HD6 comprise an Arg and an Asn residue respectively, coordinating the guanine base, while HD4 contains a Glu and Asp pair which is proposed to facilitate the nucleophilic attack on the 3′-phosphate group of the substrate (23, 43). Finally, HD2 (His), HD3 (His and Asp), and HD5 (Asp and Arg/Lys) are involved in manganese ion coordination (23, 42, 43). Curiously, the first SAH structures determined were of the metazoan ortholog Mesh1 from human and *Drosophila melanogaster* ($Mesh1_{Hs}$ and $Mesh1_{Dm}$, respectively), which were shown to possess (p)ppGpp hydrolase activity both *in vitro* and *in vivo* (43). The discovery of a metazoan alarmone hydrolase was initially surprising, as no role for alarmones had been identified in higher organisms at the time. Later, Mesh1 was shown to function as a NADPH phosphatase required in development and ferroptosis-mediated cell death caused by metabolic starvation (44). Recently, the first structure of a bacterial SAH from *Pseudomonas aeruginosa* (*Pa*SAH) was reported (42). *Pa*SAH is also capable of degrading (p)ppApp and required for biofilm formation (45), expanding its function to interbacterial growth competition. Finally, members of the Nudix family, which are known for their substrate ambiguity (46), have also been shown to be involved in alarmone degradation and nucleotide homeostasis both in plants (47) and bacteria (19, 48, 49).

In this article, we present crystal structures of two unique SAH enzymes from *Corynebacterium glutamicum* ($RelH_{Cg}$) and *Leptospira levettii* ($RelH_{Ll}$) and show that both enzymes are catalytically active as dimers. Using this information and through comparison with the bifunctional RSHs, we reveal conserved structural features unique to the monofunctional SAHs. We observe that dimerization is a general feature of bacterial SAHs but that the exact mode of dimer conformation varies, which might influence regulation or stability, or both, in diverse bacterial species. Furthermore, we show that $RelH_{Cg}$ is subject to product-dependent inhibition by GTP/GDP. $RelH_{Ll}$ is less active than $RelH_{Cg}$ and does not seem significantly affected by its products, potentially instead relying on active site accessibility for regulation. Our results suggest that regulatory mechanisms differ between bacterial species and may be controlled by the type of dimer formed. We therefore propose that SAHs evolved to form homodimers with diverse dimerization interfaces and regulation mechanisms, likely linked to the maintenance of GTP/GDP homeostasis in some bacteria.

Results

The SAH of C. glutamicum *forms a dimer*

To better understand SAH function and regulation, we decided to determine the crystal structure of the most well-characterized member of the SAH family, *C. glutamicum*, $RelH_{Cg}$ (*cg1485/cgl1313*, 188 amino acids, UniProt ID: Q8NQV9) (50, 51). The structure was determined using seleno-methionine (Se-Met)–derivatized protein by the single wavelength anomalous diffraction method at 2.3 Å in the primitive hexagonal space group, $P6_3$. This model was then transferred to a higher resolution 1.8 Å native dataset that was used to build the final model. The final structure has R_{work} = 17.6% and R_{free} = 20.5% (see Table 1 for data collection and refinement statistics). The asymmetric unit contains two nearly identical molecules of $RelH_{Cg}$ (Fig. 1*A*) of which one (chain A) was fully traced to the C-terminus (A188), including the linker and the first two residues of the histidine affinity tag to H192. The second molecule (chain B) could be traced to L185, except for a loop region (145–148) connecting helix α8 and α9. The structure reveals a core fold of ten α-helices with a cavity open to solvent where the active site of the HD domain is located (Fig. 1*A*) (24). All conserved residues typically involved in the hydrolase activity (R24, H34, H58, D59, E62, D63, D122, K123, and N126) are located inside this cavity (Fig. 1, *A* and *B*) of which R24 and N126 (motifs HD1 and HD6) are expected to coordinate the guanine base of the substrate alarmone. R24, which is responsible for π-stacking interactions with the base (23, 31, 42), is observed in two alternative conformations in our structure, probably reflecting the lack of substrate in the active site (Fig. 1*B*). At the center of the active site cavity, H34, H58, D59, and D122 (the HD2, HD3 and HD5 motifs) coordinate a divalent cation necessary for hydrolase activity (Fig. 1, *B* and *C*) (24). A strong positive electron density in the anomalous difference map at this site suggests this ion is Mn^{2+} (Fig. 1*C*), consistent with the presence of this ion in the crystallization buffer. Moreover, two well-ordered waters completing the octahedral coordination shell are clearly visible (Fig. 1*C*). E62 and D63 (motif HD4) are known to be involved in the nucleophilic attack on the nucleotide 3′-phosphate (23). Closer inspection of the interaction surface between the two molecules in the asymmetric unit reveals a pocket containing a set of hydrophobic residues typical of protein interfaces. Analysis of the protein contacts in the crystal using the PISA (Proteins, Interfaces, Structures, and Assemblies) server (52) revealed an interface with a total buried area of ∼1286 $Å^2$, consistent with a homodimer of biological relevance. Finally, to obtain a ligand-bound structure of the enzyme, we next crystallized both WT protein as well as several inactive mutants (E62N, D63N, N126D, N126L, and R24Q) of $RelH_{Cg}$ in presence of substrate (pppGpp or ppGpp) or product (GTP, GDP) at molar ratios of 1:3 to 1:5 (protein:ligand). However, these experiments produced poorly diffracting crystals of insufficient quality to allow structure solution.

$RelH_{Cg}$ and $RelH_{Ll}$ form structurally distinct dimers

To understand if dimerization is a unique characteristic of $RelH_{Cg}$ or a more general feature of SAHs, we selected a homolog from the gram-negative bacterial species *L. levettii* (*CH368_08595*, 196 amino acids, UniProt ID: A0A2N0AXP5) as our target for further study. We obtained crystals of $RelH_{Ll}$

Table 1
Crystallographic data collection and refinement statistics

Structure	Se-Met $RelH_{Cg}$	$RelH_{Cg}$	$RelH_{Ll}$
PDB ID	7QOC	7QOD	7QOE
Data collection			
Wavelength (Å)	0.97624	0.97624	0.97624
Resolution range	41.6–2.3 (2.38–2.3)	36.1–1.85 (1.92–1.85)	37.1–1.2 (1.24–1.2)
Space group	P 6_3	P 6_3	P 4_2 2_1 2
Unit cell dimensions			
a, *b*, *c* (Å)	96.0, 96.0, 80.4	94.3, 94.3, 80.5	98.7, 98.7, 40.0
α, *β*, *γ* (°)	90, 90, 120	90, 90, 120	90, 90, 90
Number of reflections			
Total	219,256 (21,902)	282,317 (27,607)	1,146,297 (114,025)
Unique	18,837 (1868)[a]	34,460 (3372)[a]	62,321 (6115)[a]
Multiplicity	11.6 (11.7)[a]	8.2 (8.2)[a]	18.4 (18.6)[a]
Completeness (%)	99.9 (99.8)[a]	99.0 (98.3)[a]	99.9 (99.7)[a]
Anomalous completeness (%)	99.9	98.5	99.6
Mean I/sigma(I)	21.2 (1.0)[a]	12.3 (1.1)[a]	16.7 (0.6)[a]
R-meas (%)	6.8 (192.9)	9.6 (192.8)	7.2 (469.1)
$CC_{1/2}$ (%)	99.9 (60.9)	99.8 (50.1)	99.9 (51.7)
CC[a] (%)	100 (87.0)	99.9 (81.7)	100 (82.5)
Refinement			
Number of used reflections			
Total	18,826 (1865)	34,449 (3372)	62,272 (6099)
Free set	942 (93)	1722 (169)	3117 (306)
R-work (%)	19.5 (32.5)	17.7 (31.1)	15.6 (45.2)
R-free (%)	21.8 (42.9)	20.6 (33.7)	18.3 (43.9)
Number of atoms			
Macromolecules	3129	3093	1611
Ligands	2	15	1
Solvent	15	107	223
RMSD from ideality			
Bond lengths (Å)	0.013	0.009	0.005
Bond angles (°)	1.51	1.01	0.79
Ramachandran statistics			
Favored (%)	98.1	98.4	99.5
Allowed (%)	1.9	1.6	0.5
Outliers (%)	0	0	0
Rama-z score overall	−0.29 ± 0.38	0.30 ± 0.39	0.27 ± 0.52
Mean atomic B-values ($Å^2$)			
Overall	90.0	51.5	28.2
Macromolecules	90.1	51.6	26.4
Ligands	100.0	57.9	17.1
Solvent	69.9	47.2	40.7

Values in parentheses represent the highest resolution shell.
[a] The data was treated and models refined against anomalous data, indicated values account for merged Friedel pairs.

in the primitive tetragonal space group $P4_22_12$ that diffracted to 1.2 Å resolution and were able to determine the structure by molecular replacement using the $RelH_{Cg}$ monomer as a search model and refine the structure to R_{work} = 15.6% and R_{free} = 18.3% (Fig. 1*D* and Table 1). In this crystal form, there is a single monomer of $RelH_{Ll}$ in the asymmetric unit, but analysis by PISA (52) reveals a dimer interface across the crystallographic two-fold axis, larger than the one observed in $RelH_{Cg}$, with a total buried surface of ∼1761 $Å^2$. To experimentally confirm the structural observation that both proteins form dimers, we used size-exclusion chromatography–multi-angle light scattering and obtained solution masses of 43.1 kDa for $RelH_{Cg}$ and 44.4 kDa for $RelH_{Ll}$ (Fig. 1*E*). As the proteins have monomeric masses of 22.4 kDa ($RelH_{Cg}$) and 23.3 kDa ($RelH_{Ll}$), these results are consistent with homodimers in both cases. Moreover, slightly different elution volumes for $RelH_{Cg}$ (11.0 ml) and $RelH_{Ll}$ (10.6 ml) are consistent with the different Stokes radii assumed by the two dimers.

Comparison of the $RelH_{Cg}$ and $RelH_{Ll}$ monomers shows a high degree of structural similarity, with an identical active site conformation (Figs. S1 and S2*A*). For $RelH_{Ll}$, Mn^{2+} was not added to the purification or crystallization buffers, nevertheless, we still observe an anomalous density peak compatible with a manganese ion in the active site metal coordination pocket (Fig. S2*B*), suggesting that this ion was carried over from the expression host. As in the case of $RelH_{Cg}$, attempts to crystallize WT or inactive mutants (D71A, N137L, or R32Q) of $RelH_{Ll}$ in presence of nucleotides did not yield crystals with sufficient diffraction. Both the $RelH_{Cg}$ and $RelH_{Ll}$ dimers are stabilized by a strongly hydrophobic interface generated by the N-terminal helices α1, α2, and α3 (Fig. 2*A*). In $RelH_{Cg}$, this core is centered on four interfacing tyrosine residues consisting of Y36 and Y40 from each molecule, plus other surrounding hydrophobic amino acids (Fig. 2*A*, top and Fig. 2*B*). The two tyrosine residues are not conserved in $RelH_{Ll}$ where they are substituted by L44 and S48 (Fig. 2*B*). Thus, the hydrophobic core of $RelH_{Ll}$ involves different amino acids and the dimer has an overall different conformation (Fig. 2*A*, bottom and Fig. 2*B*). Moreover, while the substrate cavities open up on the same side of the dimer surface in $RelH_{Cg}$, the monomers are rotated 180° with the substrate cavities exposed on opposite sides of the dimer in $RelH_{Ll}$ (compare Figs. 1*A* and 1*D*). In $RelH_{Ll}$, F16, L20, and L44 are located at the center of the dimeric helical arrangement and form a hydrophobic core (Fig. 2*A*, bottom left). As

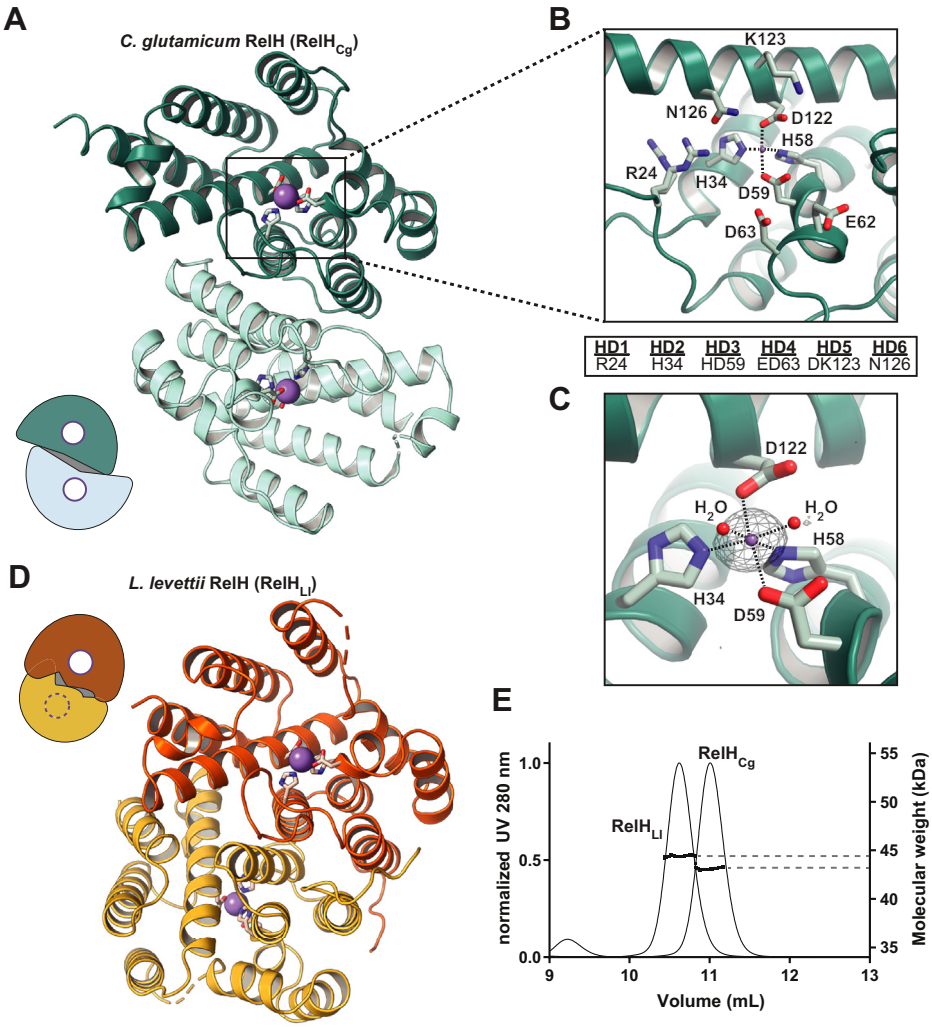

Figure 1. Overall structures and active site configuration in the RelH$_{Cg}$ and RelH$_{Ll}$ small alarmone hydrolases. *A*, overview structure of the *Corynebacterium glutamicum* RelH$_{Cg}$ dimer, with single monomers colored in *dark* and *light teal*, respectively. The Mn^{2+} ion in the active site is shown as a *purple sphere* with the coordinating residues depicted as *sticks*. The small schematic highlights the position of the active site cavities (*white circles*) and the interaction interface (*gray area*). *B*, close-up view of the active site of RelH$_{Cg}$. All residues that form a part of the six HD motifs necessary for hydrolysis are shown as *sticks* and reported in the small box. The Mn^{2+} ion is shown as a *small purple sphere*. R24 was observed in two alternative conformations. *C*, the Mn^{2+} ion coordination shell with the anomalous electron density map shown as a *gray mesh* and contoured at 3.5 σ. The ion (in *purple*) is coordinated with octahedral geometry by H34, D122, H58, and D59 and two waters molecules (shown as *red spheres*). *D*, overview structure of the *Leptospira levettii* RelH$_{Ll}$ dimer with the monomers colored in *dark* and *light amber*, respectively. The structure is rotated in such a way to align the top monomer to the respective top monomer in RelH$_{Cg}$. The Mn^{2+} ion in the active site is shown as a *purple sphere* with the coordinating residues as *sticks*. The small schematic highlights the position of the active site cavity (*white circle*) and the interaction interface (*gray area*). *E*, molecular mass determination of RelH$_{Cg}$ and RelH$_{Ll}$ by SEC-MALS. RelH$_{Cg}$ eluted at 11 ml with a measured mass of ∼43.1 kDa, whereas RelH$_{Ll}$ eluted at 10.6 ml with a measured mass of ∼44.4 kDa, in both cases closely matching a dimer. HD, hydrolase domain.

the replacement of Y36 and Y40 of RelH$_{Cg}$ with L44 and S48 in RelH$_{Ll}$ represents one of the major differences of their hydrophobic dimerization interfaces, we probed the importance of the tyrosine residues for dimer formation by generating a RelH$_{Cg}$ Y36E-Y40E double mutant to destabilize the dimer interface by electrostatic repulsion and drive the equilibrium toward monomers. The resulting protein was not soluble, suggesting that dimerization is likely required for protein stability and thus, natural function of the enzyme.

Outside of its hydrophobic core, RelH$_{Cg}$ has only one notable dimer interaction between R9 of helix α1 from one monomer and D132 of α7 from the other (Fig. 2*A*, top right). These residues are replaced by glycine and serine in RelH$_{Ll}$, respectively, and do not interact (Fig. 2*B*). Instead, the interaction interface of RelH$_{Ll}$ extends between helices α7, α10, and α2. This region contains several polar residues creating a network of hydrogen bonds and salt bridges between the monomers (Fig. 2*B*). At its center, R139 from each monomer forms a π-stacking interaction with the corresponding residue from the other molecule, which is supported and kept in position by E186 of the same monomer (Fig. 2*A*, bottom right). Except for E52, which is located on α2, all other residues involved in electrostatic interactions for dimer formation are located at the C-terminus of RelH$_{Ll}$ (Fig. 2*B*). Of the nine residues involved in helices α7 and α10, H136, S140, D144, R182, and E186 of RelH$_{Ll}$ are conserved between the two hydrolases (Fig. 2*B*), but intriguingly they do not form dimer contacts in RelH$_{Cg}$. Furthermore, R182 belongs to helix

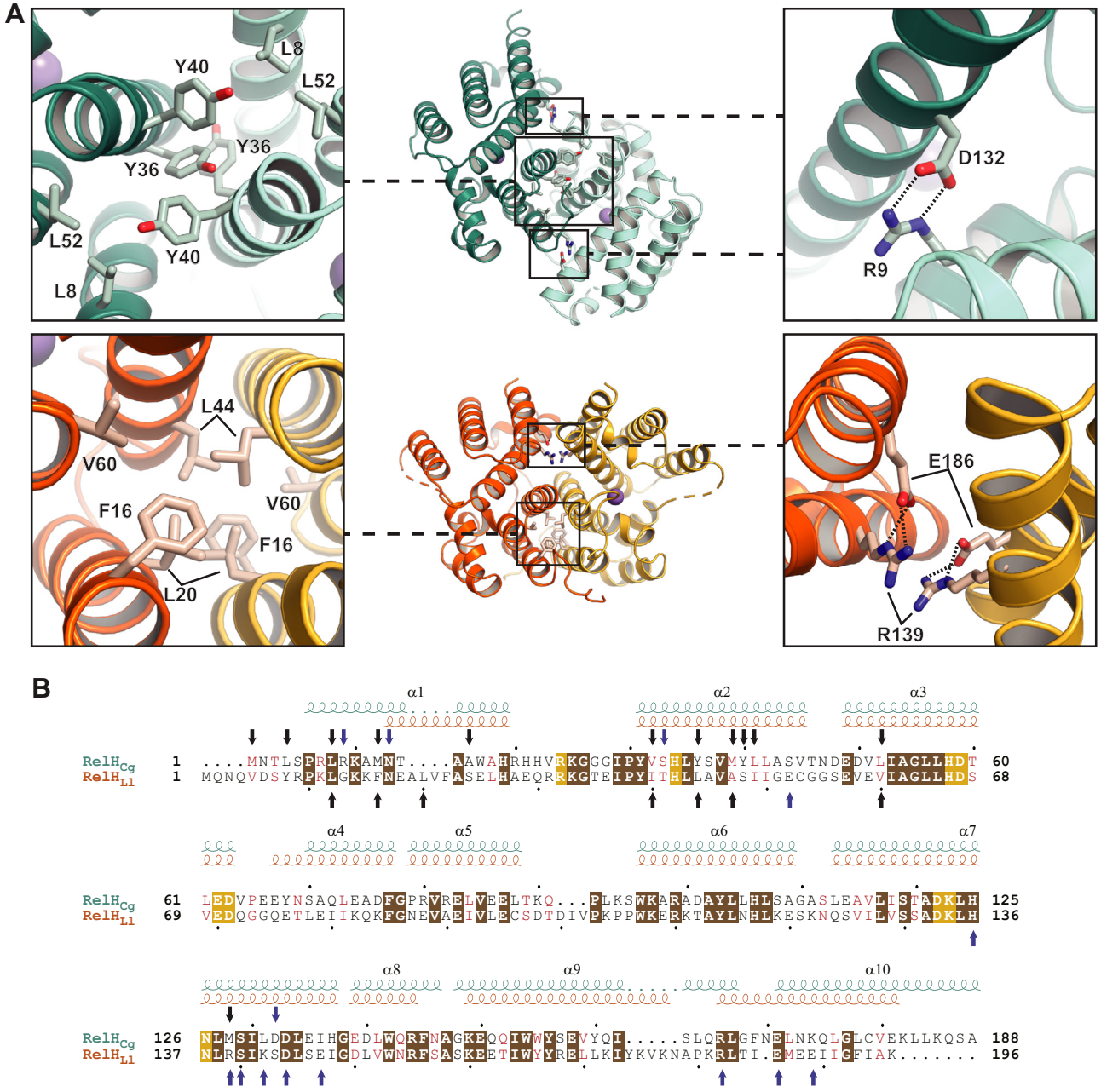

Figure 2. Dimerization interfaces and sequence comparisons of $RelH_{Cg}$ and $RelH_{Ll}$. *A*, comparison of the $RelH_{Cg}$ (*teal*) and $RelH_{Ll}$ (*amber*) dimers and close-up views of their respective dimerization interfaces. A selected subset of residues involved in the interaction are highlighted as *sticks* and labeled. At the center, the top monomers are aligned to highlight the differences in dimer formation. *Left*, hydrophobic dimer interfaces in $RelH_{Cg}$ (*top*) and $RelH_{Ll}$ (*bottom*), respectively; *right*, inter-subunit electrostatic interactions found in $RelH_{Cg}$ and $RelH_{Ll}$, respectively. *B*, pairwise sequence alignment of $RelH_{Cg}$ and $RelH_{Ll}$ with indication of secondary structure shown in *teal* ($RelH_{Cg}$) and *amber* ($RelH_{Ll}$). *Black dots* indicate every 10th residue of each sequence. Identical residues are shown in *white* on a *brown background*, while residues with similar chemical properties are shown in *red*. Active site residues are shown in *white* on a *gold background*, and *black arrows* indicate hydrophobic residues involved in interactions at the dimer interfaces. Finally, *blue arrows* indicate polar residues involved in electrostatic interactions.

α10 of $RelH_{Ll}$, while R166 of $RelH_{Cg}$ belongs to helix α9. The remaining four of the corresponding residues of $RelH_{Cg}$ are substituted with side chains that are either hydrophobic or of opposite charge. Thus, the conformational differences of the interaction interfaces of $RelH_{Cg}$ and $RelH_{Ll}$ allow for the major deviation between the positions of the respective monomers observed and their substrate cavity in the two enzymes.

To test the recent developments in protein structure prediction against our findings, we generated prediction models of currently deposited SAH structures, $RelH_{Cg}$ and $RelH_{Ll}$ using the AlphaFold-Multimer system of AlphaFold2 (53) under the assumption that they can dimerize. This list includes *P. aeruginosa* SAH (*Pa*SAH, PDB ID: 6YVC) (42), the metazoan orthologs Mesh1 from human ($Mesh1_{Hs}$, PDB ID: 3NR1 and 5VXA) and *D. melanogaster* ($Mesh1_{Dm}$, PDB ID: 3NQW) (43, 44), and the unpublished putative SAH from *Listeria monocytogenes* ($RelH_{Lm}$, PDB ID: 4YF1). Five models were created for each SAH (Fig. S3). We observed that the predicted

models of $RelH_{Cg}$, $RelH_{Ll}$, *Pa*SAH, $Mesh1_{Hs}$, and $Mesh1_{Dm}$ had very high local and global confidence prediction (Fig. S4, *A–C*, *E* and *F*) and converged to dimers that aligned to PISA-predicted dimers from experimental crystallographic data with low RMSD values for the Cα backbone ranging from ∼0.3 to ∼0.8 Å (Table S1 and Fig. S3). The predicted $RelH_{Lm}$ models, however, had good local confidence but showed poor predicted alignment error scores instead, indicating that the relative orientation of the domains is unreliable (Fig. S4*D*). Furthermore, the predicted $RelH_{Lm}$ dimers did not converge toward any singular dimer conformation and all predicted conformations were different from those observed in the crystal structure (Fig. S3 and Table S1). We believe that these results highlight that AI-based protein structure prediction, particularly when involving intermolecular contacts, should go together with experimental verification to avoid pitfalls.

$RelH_{Cg}$ is a highly efficient hydrolase limited by product-dependent inhibition

To understand if the SAH enzymes are active as dimers, we purified the proteins on their dimer forms and carried out *in vitro* hydrolysis reactions in which we separated the substrate alarmones (p)ppGpp from their GTP/GDP products by ion exchange chromatography (Fig. S5). In time course experiments, the concentrations of each enzyme were adjusted to 0.05 μM for $RelH_{Cg}$ and 2.5 μM for $RelH_{Ll}$ to achieve measurable hydrolysis curves and better estimate initial rates. For $RelH_{Cg}$, we observed specific activities of 0.59 μmol/min/mg (pppGpp) and 2.23 μmol/min/mg (ppGpp). Notably, only ∼50% pppGpp was hydrolyzed after 180 min (Fig. 3*A*, left). In contrast, $RelH_{Ll}$ showed similar rates of pppGpp and ppGpp hydrolysis but was overall much less efficient than $RelH_{Cg}$. In this case, we observed specific activities of 0.039 μmol/min/mg (pppGpp) and 0.026 μmol/min/mg (ppGpp). Unlike $RelH_{Cg}$, $RelH_{Ll}$ was able to hydrolyze up to 90% of total pppGpp, at a slightly higher rate for pppGpp compared to ppGpp (Fig. 3*A*, right).

It has previously been observed that >500 μM substrate (alarmone) concentrations can inhibit $RelH_{Cg}$ (50), however, those findings do not explain the observations in our experimental setting, where we observe a clear reduction of pppGpp hydrolysis activity over time in $RelH_{Cg}$ starting from an alarmone concentration of 50 μM (Fig. 3*A*, left). To check for regulation by nucleotides, we next decided to study the effect of presence of the products GTP and GDP on the hydrolysis reaction. Upon increasing the concentration of GTP, we observed a clear inhibition of alarmone degradation by $RelH_{Cg}$ (Fig. 3*B*, left). GDP also seems to have an inhibitory effect, although weaker than GTP, most noticeable against ppGpp hydrolysis in presence of 400 μM GDP (Fig. 3*C*, left). In the case of $RelH_{Ll}$, only ppGpp hydrolysis appeared to be affected by 400 μM GTP, while addition of GDP had only a minimal effect (Fig. 3*C*, right).

To determine if product inhibition of $RelH_{Cg}$ and $RelH_{Ll}$ is competitive or allosteric, we used the differential radial capillary action of ligand assay (DRaCALA), which measures small molecule affinity in the presence of an antagonist (54–56). A one-way ANOVA was conducted to assess if cold antagonists influenced the fraction of binding of radiolabeled nucleotides. A post-hoc Dunnett's multiple comparison test was then performed where an effect was observed, to determine if there were significant differences between each cold nucleotide and the buffer control. After binding of radiolabeled GTP (α-^{32}P-GTP) to $RelH_{Cg}$, we observed reduced binding fractions of α-^{32}P-GTP upon incubation with cold GTP, GDP, pppGpp, or ppGpp ($p < 0.0001$) (Fig. 4*A*, left) suggesting that these compounds can displace bound α-^{32}P-GTP and thus compete directly with GTP for binding. $RelH_{Ll}$ showed no evidence of binding α-^{32}P-GTP in the first place (Fig. 4*A*, right), consistent with the lack of product inhibition in Figure 3*B*, right. Moreover, pppGpp ($p = 0.0104$) and ppGpp ($p = 0.0111$), but not GTP or GDP, significantly reduced the binding of radiolabelled pppGpp (α-^{32}P-pppGpp) to $RelH_{Cg}$ (Fig. 4*B*, left). Similarly, pppGpp ($p = 0.0378$) and ppGpp ($p = 0.0050$) significantly reduced binding of α-^{32}P-pppGpp binding to $RelH_{Ll}$ (Fig. 4*B*, right). It should be noted, however, that the fraction of α-^{32}P-pppGpp binding might be influenced by the enzymatic activity of $RelH_{Cg}$ and $RelH_{Ll}$. Nevertheless, these data suggest that the nucleotide products, GTP and GDP, compete for the active site binding with alarmone to $RelH_{Cg}$, while they did not show a significant effect on $RelH_{Ll}$ in this setup.

Monofunctional SAHs contain structural elements absent in bifunctional RSHs

Despite their differences, dimerization of $RelH_{Cg}$ and $RelH_{Ll}$ in both cases involves the N-terminal part of the protein. The hydrophobic pocket formed by helices α1, α2, and α3 at the dimerization interface of SAHs is structurally present in bifunctional RSHs but is obscured by an additional N-terminal helix, as observed in example Rel from *Streptococcus dysgalactiae* subsp. *equisimilis* (Rel_{Seq}, PDB ID: 1VJ7) (23). This N-terminal helix buries the hydrophobic residues that would otherwise be exposed and thus compensates for the lack of a dimeric interface to shield these residues from solvent (Fig. S6). Similar structural patterns are observed in the structures of Rel_{Th} from *Thermus thermophilus* (PDB ID: 6S2T, 6S2U, 6S2V) (31), BsRel from *B. subtilis* (PDB ID: 6YXA) (40), and MtRel from *Mycobacterium tuberculosis* (PDB ID: 5XNX) (41).

The positions of helices α5 and α6 (corresponding to α6 and α7 in bifunctional Rel enzymes) also differ between monofunctional SAHs and bifunctional RSHs. Upon substrate binding in the synthetase domain of the bifunctional Rel_{Th}, helix α7 undergoes a massive conformational rearrangement, switching the entire enzyme from the hydrolase-ON/synthetase-OFF to the hydrolase-OFF/synthetase-ON state (31). This shift results in movement of a loop (residues 108–121 of Rel_{Th}) toward the hydrolase active site, placing Y111 at the guanine base position, effectively preventing substrate access and thus rendering the hydrolase domain inactive. Interestingly, the corresponding α6 helix in both $RelH_{Cg}$ and $RelH_{Ll}$ is found in a conformation closer to the hydrolase-OFF state of Rel_{Th}, contrary to what might be expected given that the enzymes are active in the crystallized form (Figs. 5*A* and S1). The long α7 helix, which is connected

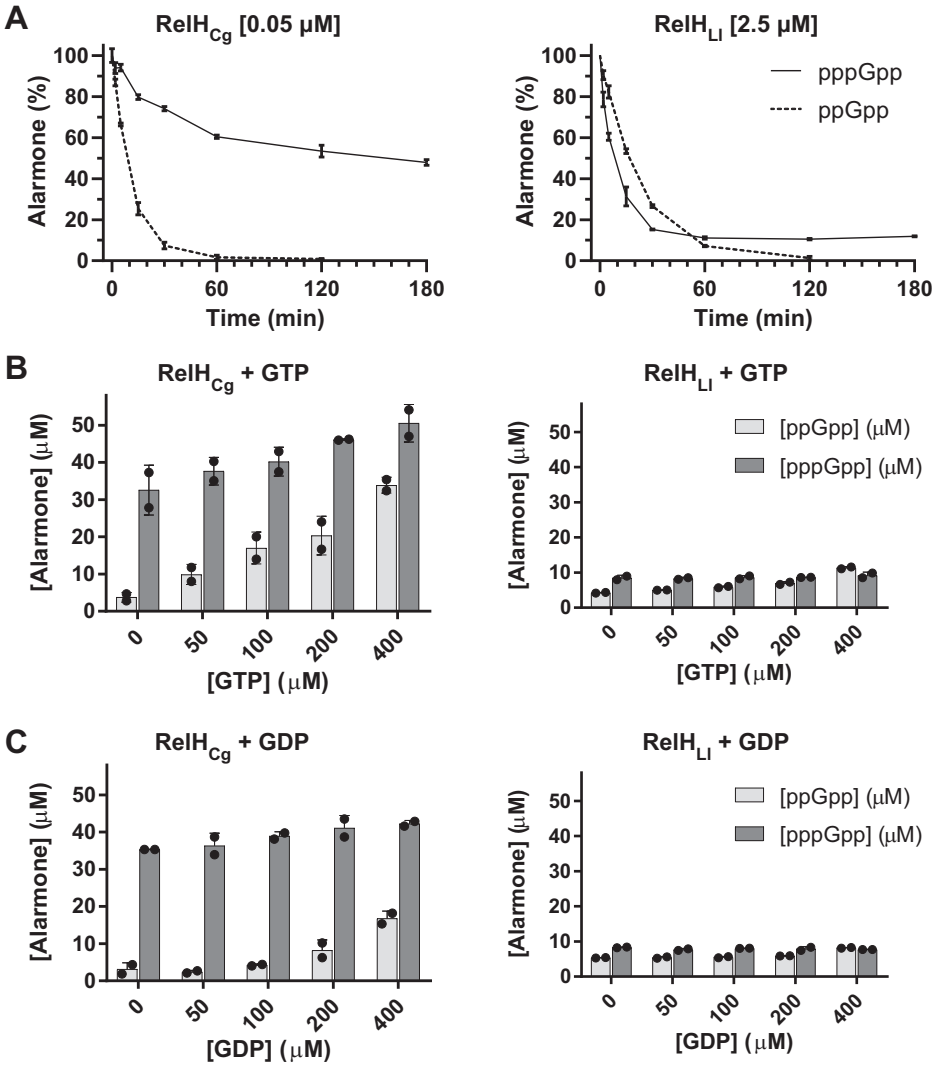

Figure 3. Both RelH$_{Cg}$ and RelH$_{LI}$ are active alarmone hydrolases *in vitro*. *A*, alarmone hydrolase activity for RelH$_{Cg}$ (*left*) and RelH$_{LI}$ (*right*) measured by the reduction in peak area of 50 μM pppGpp (*solid line*) and ppGpp (*dashed line*) following separation by anion exchange chromatography. Measurements were performed in triplicate after incubation for 0, 2, 5, 10, 15, 30, 60, and 120 min for both alarmones and additionally at 180 min for pppGpp. The points represent the averages with *black bars* showing SDs. *B*, concentrations of ppGpp (*light gray bars*) and pppGpp (*dark gray bars*) measured after 60 min hydrolysis in presence of RelH$_{Cg}$ (*left*) and RelH$_{LI}$ (*right*) and increasing concentrations of GTP as indicated. *Bars* represent the averages of two independent experiments at each concentration with *black lines* showing SDs. Single measurements are shown as *black dots*. *C*, as in *B* but including GDP from 0 to 400 μM. ppGpp, guanosine 3′,5′-bis(diphosphate); pppGpp, guanosine 3′-diphosphate 5′-triphosphate.

to the downward facing α9 helix *via* the perpendicular α8 (residues 137–148 in RelH$_{Cg}$), is found in the monofunctional RelH$_{Cg}$, RelH$_{Ll}$, and RelH$_{Lm}$ structures. In the bifunctional Rel$_{Seq}$, Rel$_{Th}$, BsRel, and MtRel, on the other hand, the corresponding α7 helix is shorter and is connected to the downward helix by a flexible loop, instead of another helix (Fig. 5*B*). This is not unique to bifunctional RSHs, though, as the metazoan SAH orthologs Mesh1$_{Ds}$ (PDB: 3NR1, 3NQW), Mesh1$_{Hs}$ (PDB: 5VXA), as well as the bacterial *Pa*SAH (PDB: 6YVC), all are reminiscent of the bifunctional enzymes, with a short helix and a connecting loop.

The active site of SAHs is conserved with bifunctional bacterial Rel enzymes

Sequence-wise, bifunctional RSHs and SAHs show great differences with the exception of the core active site residues, which are highly conserved as would be expected given that they catalyze identical reactions (Fig. 6) (20). Examination of the key differences in residues reported to be involved in substrate coordination and activity (23) reveals that the HD1 motif (R44) of bifunctional Rel$_{Seq}$ (23), which is involved in π-stacking with the guanine base of (p)ppGpp, is well conserved in both monofunctional and bifunctional enzymes, with the notable exception of SAH from *P. aeruginosa* (*Pa*SAH), where it is substituted for leucine (42) (Fig. 6). Interestingly, while mutation of this arginine to glutamate (R44Q) inactivates the hydrolase activity of Rel$_{Seq}$ (23), *Pa*SAH remains active with a Leu at this position (42). In the selected set of SAH sequences, the HD1 Arg is often substituted for Asp, which frequently coincides with another substitution in the HD5 domain, where a D:R/K pair is replaced by D:Φ (where Φ is any hydrophobic amino acid) (Fig. S7). It is currently unknown whether these differences influence

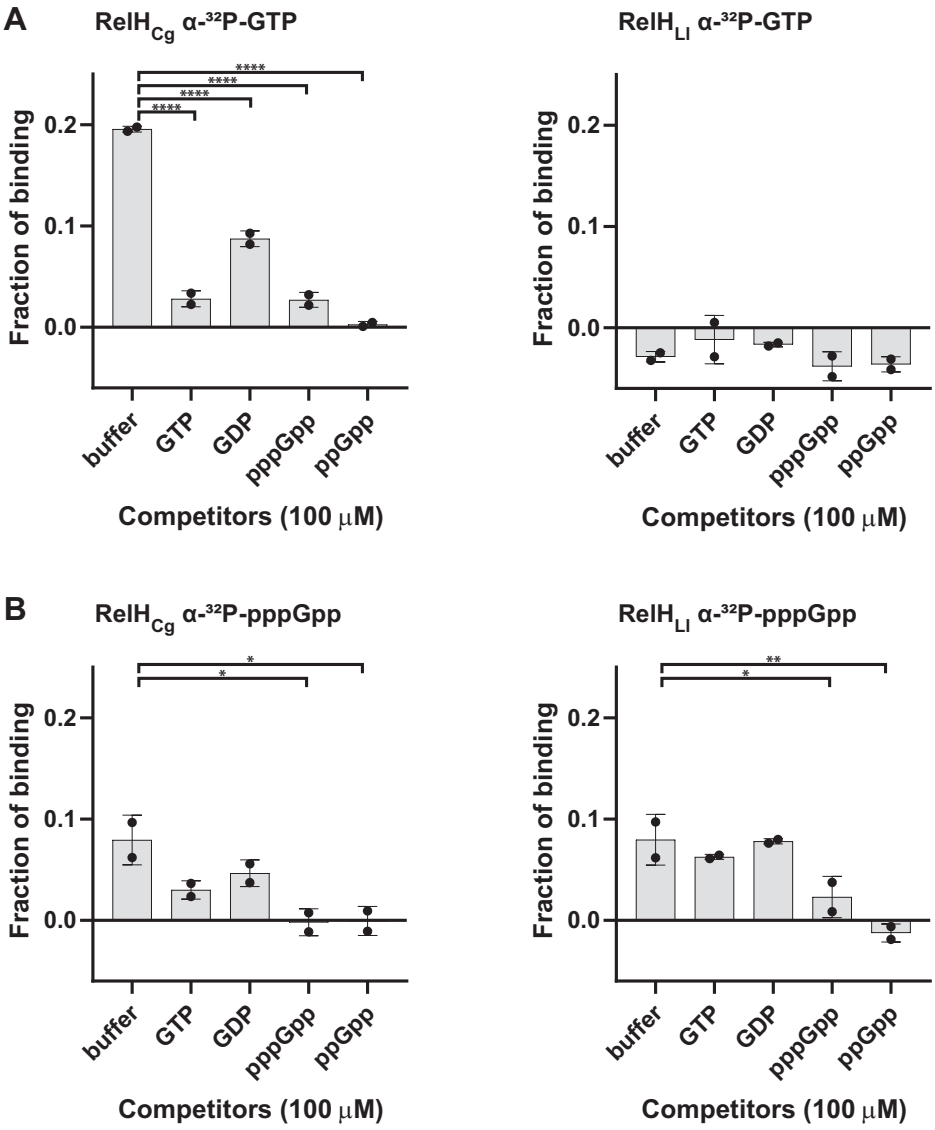

Figure 4. Nucleotide competition assay. *A*, measurement of the binding fraction of radioactive α-^{32}P-GTP to RelH$_{Cg}$ (*left*) and RelH$_{Ll}$ (*right*) in the presence of buffer or when challenged by 100 μM cold competitor, as indicated. The *bars* show the average of two independent experiments with SD. Single experiments are shown as *black dots*. *B*, as in *A* but measured for the binding of α-^{32}P-pppGpp. Statistically significant differences in the fraction of binding between cold competitors and buffer controls are shown as indicated: *$p \leq 0.05$, **$p \leq 0.01$, ****$p \leq 0.0001$. pppGpp, guanosine 3′-diphosphate 5′-triphosphate.

activity, regulation, or both. Notably, while containing the leucine mutation at the HD1 position, the HD5 motif of *Pa*SAH is intact (Figs. 6 and S7). In Rel$_{Seq}$, the side chain of R44 (HD1) is held in place by direct H bonds to residues N148 (which forms the HD6 motif of the HD domain) and T151 when coordinating a nucleotide. The HD6 motif is clearly conserved in all examined RSHs, while T151, conserved in the bifunctional RSH we have included, is conservatively substituted for a Ser in RelH$_{Cg}$ (S129), RelH$_{Ll}$ (S140), and RelH$_{Lm}$ (S120), but not in *Pa*SAH or the Mesh1 orthologs (Fig. 6). This interaction is not present in our structures in absence of a nucleotide in the active site. Although a Ser substitution appears widespread, it is not necessarily shared by all SAHs (Fig. S7).

K45 of Rel$_{Seq}$, which forms an H bond with the substrate, appears to be maintained or conservatively substituted with Arg in most hydrolases, as in the case of bifunctional Rel$_{Th}$ (31). S46 from Rel$_{Seq}$ is described to stabilize R44 *via* a water-mediated H bond, as well as forming another H bond with the guanine base of (p)ppGpp. While Rel$_{Seq}$ S46 seems well conserved in bifunctional hydrolases (23) and is also found in the bifunctional Rel$_{Th}$ (31), it seems often substituted by hydrophobic residues or glycines in monofunctional SAHs (G26 of RelH$_{Cg}$ and G34 of RelH$_{Ll}$, Figs. 6 and S7). Additionally, the loop of which the residue is a part assumes a different position in monofunctional hydrolases compared to bifunctional RSHs, as the result of a residue insertion where G26 is followed by an additional residue (Gly in RelH$_{Cg}$, Thr in RelH$_{Ll}$, and RelH$_{Lm}$ and Ser in *Pa*SAH) (Figs. 5*C* and 6). Due to this insertion, this loop assumes two slightly different conformations when comparing monofunctional and bifunctional hydrolases (Fig. 5*C*). Furthermore, metazoan hydrolases Mesh1$_{Hs}$ and

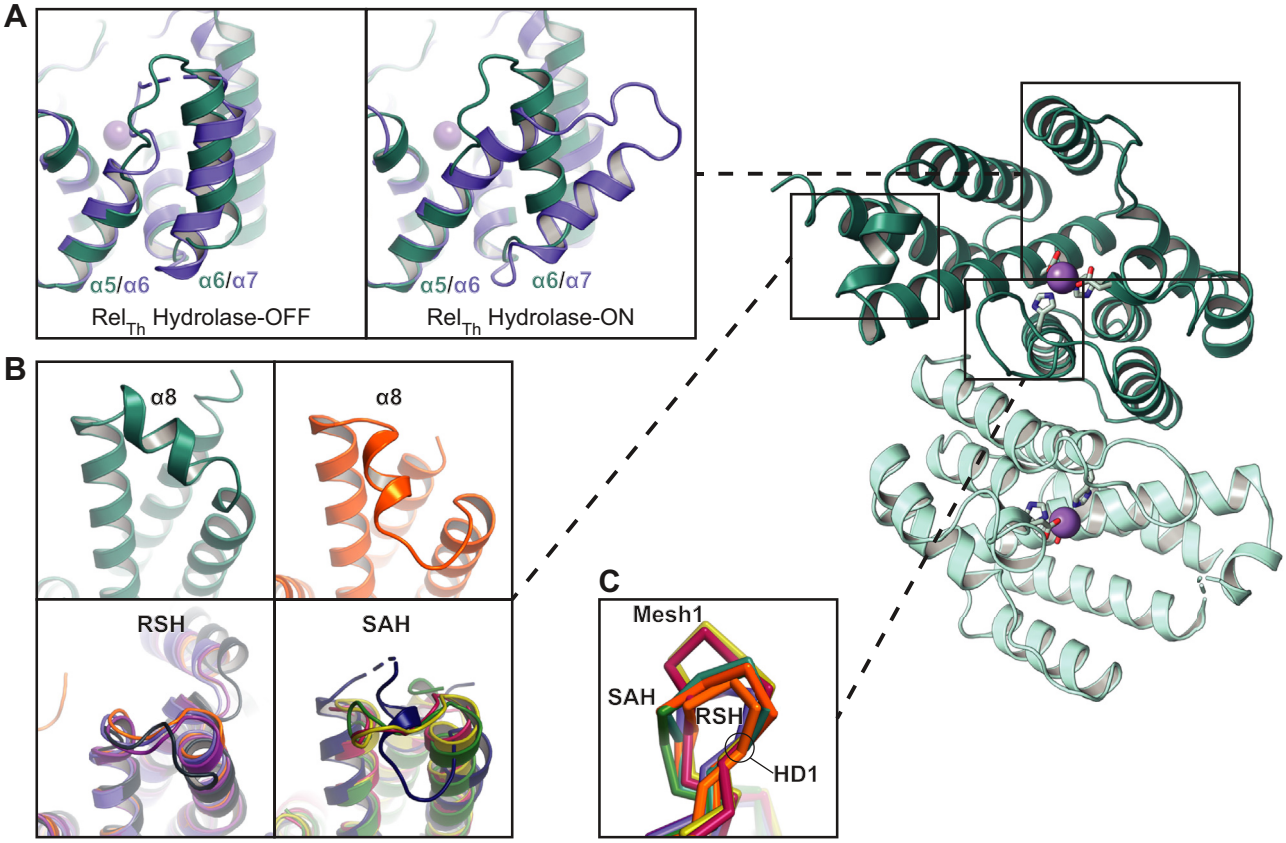

Figure 5. Structural comparisons with bifunctional hydrolases. *A*, alignment of the "switch" helix involved in the regulation of bifunctional RelH$_{Th}$ (*blue*) in the hydrolase-OFF (*left*) (PDB ID: 6S2U) and hydrolase-ON (*right*) (PDB ID: 6S2T) states (31) with RelH$_{Cg}$ (*dark teal*). Helices α5 and α6 of RelH$_{Cg}$ are indicated and correspond to α6 and α7 in Rel$_{Th}$, respectively. *B*, *top*, the conformation around helix α8 in RelH$_{Cg}$ (*dark teal*) and RelH$_{Ll}$ (*dark amber*); *bottom left*, aligned views of the bifunctional RSHs Rel$_{Seq}$ (*purple*, PDB ID: 1VJ7) (23), Rel$_{Th}$ (*blue*), MtRel (*Prussian blue*, PDB ID: 5XNX) (41), and BSrel (*orange*, PDB ID: 6YXA) (40) that have a loop at the position of this helix; *bottom right*, aligned view of the bacterial *Pa*SAH (*dark green*, PDB ID: 6YVC) (42) and the metazoan *Drosophila* and human Mesh1 (*yellow* and *dark pink*, PDB ID: 3NQW and 3NR1) (43), which also have loops, while bacterial RelH$_{Lm}$, (*dark blue*, PDB ID: 4YF1) has a helix similar to RelH$_{Ll}$. *C*, ribbon representation of the loop region around HD1, which is structurally conserved and with its position indicated. Rel$_{Seq}$ (*purple*), Rel$_{Th}$ (*blue*), and BsRel (*orange*) have the shortest loop, while bacterial RelH$_{Cg}$ (*dark teal*), RelH$_{Ll}$ (*dark amber*), and *Pa*SAH (*dark green*) have an insertion that introduces a kink and lengthens the loop after HD1. The metazoan orthologs *Drosophila* and human Mesh1 (*yellow* and *dark pink*) have one more insertion with the widest loop. HD, hydrolase domain; RSH, RelA/SpoT homolog; SAH, small alarmone hydrolase.

Mesh1$_{Dm}$ present a third distinct conformation reflected by an additional insertion compared to the bacterial SAHs (Fig. 5*C*). Although the loop containing the HD1 motif can adopt at least three distinct geometries, the position of the HD1 motif (R44 in RelSeq) itself does not differ significantly and occupies virtually the same position in all the observed geometries of the loop from the currently known structures.

Discussion

SAHs have diverse oligomerization interfaces across species

Our studies clearly show that RelH$_{Cg}$ and RelH$_{Ll}$ are active dimers in solution and since disruption of the interface causes the proteins to become unstable, this is most likely also the case inside cells (Figs. 1 and 2). In both cases, the dimerization interface mainly involves a hydrophobic region formed by the first three N-terminal helices (Fig. 2*A*). A similar hydrophobic region is also present in bifunctional RSHs but is buried by an additional N-terminal helix (Fig. S6), which prevents bifunctional enzymes from making similar interactions through this side of their hydrolase domain. Furthermore, although the hydrophobic core is still central for dimerization in RelH$_{Cg}$ and RelH$_{Ll}$, we observed two distinct dimers (Fig. 2*A*). Based on this observation, we further extended our analysis to the other SAHs currently deposited in the PDB (*Pa*SAH, Mesh1$_{Hs}$, Mesh1$_{Dm}$, and RelH$_{Lm}$). Analysis of these structures *via* PISA (52) confirmed the presence of strong dimer interfaces ranging from 1200 to 1350 Å^2, except for RelH$_{Lm}$, which only has a surface of ∼800 Å^2 but also shows other atypical characteristics, as detailed below. All dimers, except RelH$_{Lm}$, contain a hydrophobic region surrounded by three N-terminal α-helices and in some cases electrostatic interactions. Comparison of the dimers shows that they assume five distinct conformations, with the two Mesh1 homologs as the only pair of identical dimers (Fig. S8). In the unique case of RelH$_{Lm}$, we note that the position of the active site residues in the deposited model does not allow for coordination of a metal ion, which is accordingly absent. Furthermore, the first N-terminal α-helix, which is an integral component of the interaction interface in other SAHs, is not present in the deposited RelH$_{Lm}$ model, where the first 20 N-terminal amino acids that are likely to form this helix are unmodeled. Therefore, we believe that the dimer observed in the crystal structure of this protein might

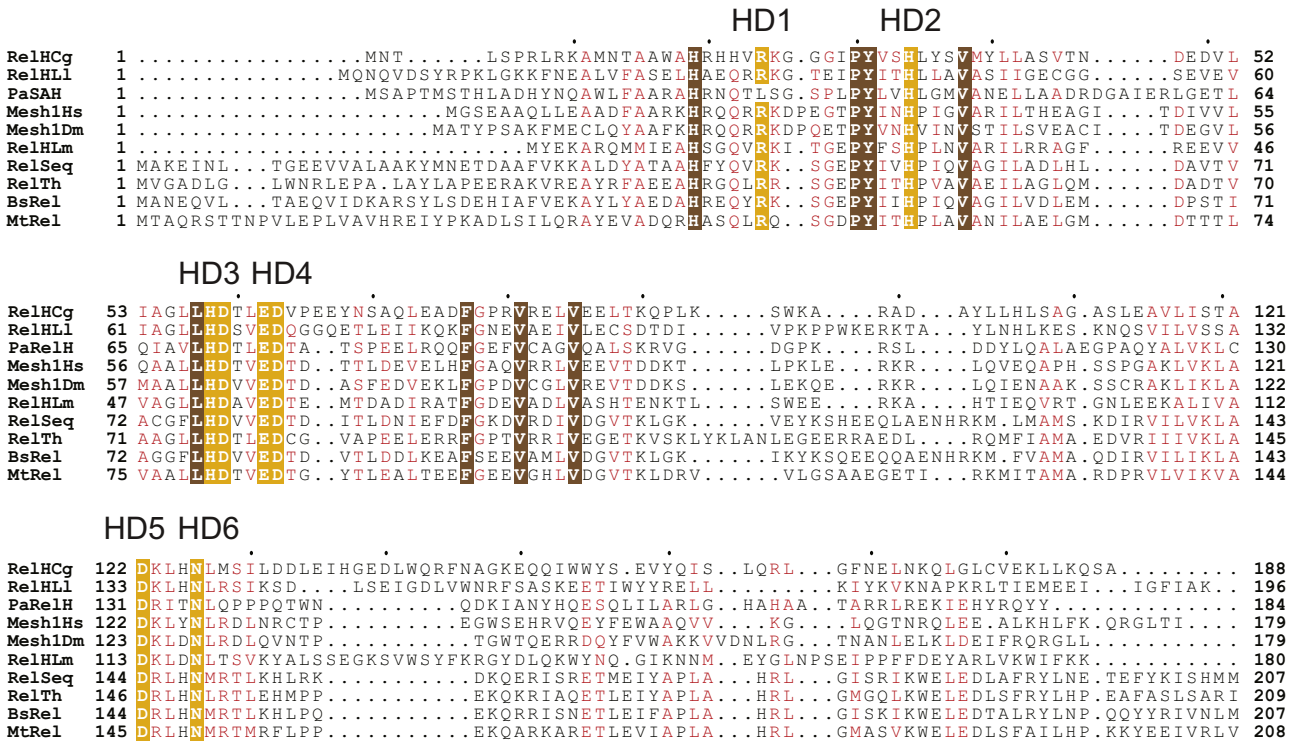

Figure 6. Sequence alignment of known SAHs and bifunctional RSHs. Structure-based sequence alignment of SAHs and bifunctional RSHs for which structures are known, created with PROMALS3D. $RelH_{Cg}$, *Corynebacterium glutamicum* RelH (UniProt ID: Q8NQV9). $RelH_{Ll}$, *Leptospira levettii* RelH (UniProt ID: A0A2N0AXP5). *Pa*SAH, *Pseudomonas aeruginosa* SAH (UniProt ID: Q9I686). $Mesh1_{Hs}$, *Homo sapiens* Mesh1 (UniProt ID: Q8N4P3-1). $Mesh1_{Dm}$, *Drosophila melanogaster* Mesh1 (UniProt ID: Q9VAM9). $RelH_{Lm}$, *Listeria monocytogenes* RelH (UniProt ID: Q8Y8T2). Rel_{Seq}, *Streptococcus dysgalactiae* subsp. *equisimilis* Rel (UniProt ID: Q54089). Rel_{Th}, *Thermus thermophilus* Rel (UniProt ID: Q5SHL3). BsRel, *Bacillus subtilis* Rel (UniProt ID: O54408). MtRel, *Mycobacterium tuberculosis* Rel (UniProt ID: P9WHG9). *Black dots* indicate every 10th residue of the top sequence ($RelH_{Cg}$). Identical residues are shown in *white* on a *brown background*, while residues with similar chemical properties are shown in *red*. Active site residues that compose the six HD domains are shown in *white* on a *gold background* with their respective motif name. HD, hydrolase domain; RSH, RelA/SpoT homolog; SAH, small alarmone hydrolase.

be an artefact, possibly due to degradation (or unfolding) of the N-terminal region.

In silico *structure prediction should be used with caution*

AlphaFold2 models support the experimentally determined dimers in all cases with high confidence, except for $RelH_{Lm}$ (Figs. S3 and S4). In the $RelH_{Lm}$ AlphaFold2 dimer prediction in particular, the proposed dimer conformations cannot be considered reliable due to poor predicted alignment error scores (Fig. S4*D*). Overall, these observations suggest that the dimers predicted by PISA in the other deposited SAHs represent the biologically relevant conformation of the proteins. While prediction models should be used with considerable caution, AlphaFold2 has already been shown to be a powerful tool that is able to predict folded protein domains with great accuracy (53, 57–60). Moreover, application to multidomain or oligomeric proteins have shown great promise, although their reliability depends on the target and critical evaluation of their confidence metrics (61, 62). Particular care should also be taken when interpreting models where transient interactions or rapidly dissociating complexes may play a biological role (63). Together with the experimental data presented here, these models support the hypothesis that dimerization of SAHs is a common characteristic across the family and it revolves around a hydrophobic patch assuming slightly different features across various species. This diversity might play an important role in the regulation and activity of these stand-alone hydrolase enzymes across bacterial species, which might or might not encode in their genome long RSHs, SASs, and/or SAHs simultaneously (20). As an example of this, we also observe significant differences in both regulation and activity for $RelH_{Cg}$ and $RelH_{Ll}$. In this way, functional regulation of SAHs would parallel the SASs, which are also regulated through multimerization, in this case through formation of tetramers as observed for both *Staphylococcus aureus* RelP and *B. subtilis* RelQ (37, 64). Furthermore, the bifunctional *M. tuberculosis* MtRel is a dimer in solution (41) and, more recently, it was shown that in *B. subtilis* BsRel dimerization is mediated through the N-terminal domain cleft formed between the hydrolase and synthetase domain and the ThrRS, GTPase, and SpoT (TGS) domain on the C-terminal side (40). Together, these observations support the notion that a common way of controlling the potentially hazardous activities of both SAHs and SASs is through multimerisation.

The activity of $RelH_{Cg}$ is controlled by a substrate-dependent competition mechanism

We observed that both SAHs were able to effectively hydrolyze ppGpp, although at different rates (Fig. 3*A*).

Interestingly, $RelH_{Cg}$ was much more efficient than $RelH_{Ll}$ but was unable to fully hydrolyze pppGpp (Fig. 3*A*). When $RelH_{Cg}$ was first characterized, inhibition of the hydrolysis reaction at alarmone concentrations above 300 to 500 μM was interpreted as substrate-dependent inhibition (50). Although our tests were conducted at only 50 μM alarmone concentration, 6- to 10-fold less, we do observe a marked reduction of pppGpp hydrolysis over time (Fig. 3*A*, left). Based on this, we hypothesize that the products GTP and GDP, rather than pppGpp, might be responsible for the reduction in activity. In support of this, our DRaCALA data suggest that both GTP and GDP have an inhibitory effect on the binding of pppGpp and ppGpp by $RelH_{Cg}$, but not $RelH_{Ll}$ (Fig. 3, *B* and *C*). Furthermore, competition experiments suggest that this inhibition is driven by substrate displacement in the active site (Fig. 4, *A* and *B*). It was previously shown that synthesis and hydrolysis of alarmones directly contribute to the homeostasis of GTP levels in *B. subtilis* (3, 65) and that perturbation has a wide range of consequences on bacterial viability (36, 66), including the possibility of causing "death by GTP" due to excessive accumulation of this nucleotide (3). Here, product-dependent inhibition might be an effective mechanism of limiting the complete and sudden degradation of alarmones, allowing to maintain control of GTP/GDP levels and fine tune the wide range of alarmone effectors with which they interact.

Active site access as a possible controller of $RelH_{Ll}$ hydrolysis

$RelH_{Ll}$ not only did not significantly respond to GTP or GDP concentrations in our experiments (Fig. 3, *B* and *C*, right and Fig. S3, *A* and *B*, right) but had considerably lower activity than $RelH_{Cg}$ (Fig. 3*A*), possibly requiring even higher concentrations of GTP/GDP for regulation, or relying on a different level of control altogether. Curiously, the remaining 10% of total pppGpp could not be hydrolyzed (Fig. 1*A*, right), although $RelH_{Ll}$ did not show clear sensitivity to GTP. Considering that $RelH_{Ll}$ and $RelH_{Cg}$ active sites are virtually identical (Fig. S2*A*) and folds are highly similar (Fig. S1), we believe that the position of helix α8 of $RelH_{Ll}$ might influence substrate binding (Figs. 5*B* and S9). Comparison of the position of ppGpp as seen in the active site of Rel_{Th} (PDB ID: 6S2T) highlights how helix α8 of $RelH_{Ll}$ partially covers the active site, bringing S157 within ∼4 Å of the β-phosphate at the 5′ position of the substrate (Fig. S9*A*). This potentially creates both steric hindrance and electrostatic repulsion at the active site access point, which would lower the affinity of (p)ppGpp. The position of helix α8 in $RelH_{Cg}$, even accounting for differences between the two monomers in our structure, allows for greater accessibility without occluding entry for the substrate (Fig. S9*B*).

Monofunctional SAHs show structural similarity to the inactive hydrolase state of bifunctional Rel enzymes

An intriguing observation is that the position of helices α5 and α6 in the SAH monomers closely resembles the described hydrolase-OFF state of bifunctional Rel_{Th} (Fig. 5*A*), despite the SAHs being active as dimers *in vitro*. In this conformation, the hydrolase active site of Rel_{Th} is occluded by a long loop and inaccessible, while the synthetase domain is active (31). However, the corresponding loop at this position in SAHs is generally shorter and, although rather flexible, it points away from the active site. Since monofunctional enzymes do not require the type of allosteric control necessary to regulate the activity of bifunctional RSHs (23, 40), a more compact and stable form might have been favored over time. Regulation of the SAHs could instead come from the α8 helix we observe in $RelH_{Cg}$ and $RelH_{Ll}$, which is not present in bifunctional Rel_{Th}, Rel_{Seq}, BsRel, and MtRel that have a simple loop (Fig. 5*B*). This, however, does not appear to be a universal feature of SAHs. In the currently known structures, three SAHs contain the α8 helix at the top of the active site ($RelH_{Cg}$, $RelH_{Ll}$, and $RelH_{Lm}$), while another three have a loop like the RSHs instead (*Pa*SAH, $Mesh1_{Hs}$, and $Mesh1_{Dm}$) (Fig. 5*B*). However, we do not yet have sufficient information to determine whether this region significantly impacts the activity of these enzymes. Finally, a potentially important detail is found at the loop where the HD1 motif is located (R44 of Rel_{Seq}). We note that while the HD1 motif position does not change, bacterial SAHs have an insertion right after, while the metazoan SAHs contain two insertions making the loop progressively longer (Fig. 5*C*). It would be highly relevant to study whether these features could affect function or regulation. Considering the importance of nucleotide homeostasis and the observation that SAHs appear constitutionally active *in vitro*, multiple levels of control might need to be investigated depending on the bacterial species involved. As for many enzymes of this type, transcriptional regulation might be the first level. Substrate accessibility, affinity, and feedback mechanisms, such as the product-dependent inhibition of $RelH_{Cg}$, are equally likely to be involved and should be studied in further detail.

Experimental procedures

Strains and plasmids

The coding sequences of WT *C. glutamicum* ATCC 13032 RelH (Q8NQV9) and *L. levettii* SAH (WP_100728644.1) were codon optimized for *Escherichia coli* expression, synthesized, and subcloned into pET22b expression vectors tagged with a C-terminal non-cleavable 6× polyhistidine tag (GenScript Biotech). Point mutants of $RelH_{Cg}$ (E62N, D63N, N126D, N126L, R24Q, Y36E-Y40E) and of $RelH_{Ll}$ (R32Q, D71A, N137L) were created by site-directed mutagenesis using Phusion high fidelity polymerase (New England Biolabs) with the primers listed in Table S2, using $RelH_{Cg}$ and $RelH_{Ll}$ WT clones as templates.

Protein expression and purification

All constructs were transformed into chemically competent *E. coli* Lemo21(DE3) cells and grown on LB agar plates in the presence of 100 μg/ml ampicillin and 34 μg/ml chloramphenicol. The $RelH_{Cg}$ construct was also transformed into the methionine auxotroph *E. coli* B834(DE3) strain for production of the Se-Met derivative protein. A 20 ml overnight culture of

each strain was diluted in 1 l of LB medium with 100 μg/ml ampicillin and 34 μg/ml chloramphenicol and grown at 37 °C until OD_{600} reached ∼0.6. With the exception of the Se-Met derivative protein, expression was induced by addition of 1 mM IPTG and incubation continued at 37 °C for 3 h. Cultures were harvested by centrifugation at 6000*g* for 15 min and the pellets collected and resuspended in a lysis buffer composed of 50 mM Hepes, pH 8, 500 mM KCl, 20 mM Imidazole, 5 mM β-mercaptoethanol.

To prepare the Se-Met derivative of $RelH_{Cg}$, bacteria were harvested by centrifugation at 3500*g* after reaching OD_{600} ∼0.6 and resuspended in minimal SelenoMethionine Medium Base (Molecular Dimensions) supplemented with methionine-less SelenoMethionine Medium nutrient mix (Molecular Dimensions), 100 μg/ml ampicillin, and 34 μg/ml chloramphenicol. The cultures were incubated at 37 °C for 3 h to deplete leftover methionine before adding Se-Met at a final concentration of 0.04 mg/ml and induction of expression with 1 mM IPTG. After 24 h, cultures were harvested and treated as previously described.

For all constructs, lysis was performed by sonication and the total lysate centrifuged at 20,000*g* for 45 min to remove cell debris. The supernatant was applied to a 5 ml HisTrap FF column (Cytiva) and washed with a buffer composed of 50 mM Hepes, pH 8, 500 mM KCl, 50 mM Imidazole, 5 mM β-mercaptoethanol. Elution was performed by increasing the imidazole concentration to 500 mM. Protein fractions were injected into a Superdex 75 Increase 10/300 GL column (Cytiva) for size-exclusion chromatography equilibrated in 20 mM Hepes, pH 8, 150 mM KCl, and 2 mM β-mercaptoethanol. The central fractions of the SEC peak were pooled and concentrated to the desired concentration for storage or further experiments using Vivaspin centrifugal concentrators (Sartorius). At each step, the quality of the sample was evaluated by SDS-PAGE on 15% polyacrylamide gels.

Crystallization

Crystallization was performed at 20 °C using the sitting-drop vapor diffusion method at a protein concentration of 10 mg/ml for $RelH_{Cg}$ and its Se-Met derivative and 8 mg/ml for $RelH_{Ll}$. Drops of 0.4 μl total volume in a 1:1 protein to precipitant ratio were set up in SWISSCI MRC 2-drop 96-well plates using the Mosquito X1 system (SPT Labtech). Initial conditions were screened on several commercial screens including the following: JCSG+, Morpheus, Midas (Molecular Dimensions), PegRX, PEG/ION, and Natrix (Hampton research). Within 24 h of incubation at 20 °C (293 K), rod-like and tetrahedral crystals were visible in several different conditions. After selection and optimization, the final crystallization condition of Se-Met $RelH_{Cg}$ was composed of 0.02 M DL-glutamic acid, 0.02 M DL-alanine, 0.02 M glycine, 0.02 M DL-lysine, 0.02 M DL-serine, 0.1 M Tris (base)-bicine pH 8.5, 20% (v/v) glycerol, 10% (w/v) PEG 4000, while $RelH_{Ll}$ crystals appeared in 0.2 M sodium acetate trihydrate, pH 7 and 20% (w/v) PEG 3350. Individual crystals of Se-Met $RelH_{Cg}$ did not need additional cryoprotection and were frozen directly. Native $RelH_{Cg}$ crystals were cryoprotected by dipping in a drop composed of mother liquor supplemented with 25% (w/v) PEG 400 and 2 mM $MnCl_2$. Crystals of $RelH_{Ll}$ were soaked in drops of a fresh buffer of the same composition as the mother liquor with the addition of 20% (v/v) glycerol. All crystals were vitrified in liquid N_2 for storage and transport before data collection.

WT and inactive mutants of $RelH_{Cg}$ and $RelH_{Ll}$ were cocrystallized or soaked in presence of GTP, GDP, pppGpp, or ppGpp. A molar ratio of 1:3 or 1:5 protein to nucleotide was used in both type of experiments. In cocrystallization experiments, protein and nucleotides were mixed and incubated 5 to 30 min before setting up crystallization drops. Upon successful crystallization, crystals were cryoprotected as previously described or in a suitable buffer with 0.5 mM of the respective nucleotide added. In soaking experiments, nucleotides were directly added to the crystallization drop or to the mother liquor, which was then applied to the crystallization drop. Finally, 0.5 mM of the respective nucleotide was added to the respective cryoprotection buffer before harvesting.

Data collection and structure solution

All data was collected from frozen crystals at 100 K at the P13 (67) or P14 beamlines of Petra III (68) using a PILATUS 6M or EIGER 16M detector, respectively at the Se x-ray peak absorption wavelength of 0.97624 Å. Data were processed in XDS (69) with XDSGUI. The first structure of $RelH_{Cg}$ at 2.3 Å resolution was determined from a Se-Met derivative crystal using the single wavelength anomalous diffraction phasing method with the CRANK2 pipeline (70) of the CCP4 suite (71, 72). High-resolution native structures of $RelH_{Cg}$ and $RelH_{Ll}$ (1.8 and 1.2 Å respectively) were then subsequently determined by molecular replacement *via* PHASER (73) of the CCP4 suite using the Se-Met structure as a search model. To build the final structures, successive iterations of refinement with phenix.refine (74) using the Phenix graphical interface (75) or Buster (76, 77) and manual building with Coot (78) were performed. At each iteration, geometry quality was validated with MolProbity (79, 80). To improve model quality of the native and Se-Met $RelH_{Cg}$ structures, translation-libration-screw rotation (TLS) domain decomposition was used to account for vibrational motion of discreet regions (81). Boundaries of each TLS group per model were determined by analysis through the TLS motion determination webserver (82). Ordered water molecules were added to all models. A density we interpret as a PEG ligand fragment was found in the map of native $RelH_{Cg}$. The ligand structure was retrieved from the PDB (PDB ID: PG4) and used in refinement along with restraints generated using Grade from the Grade Web Server (http://www.globalphasing.com) (83). In the case of the $RelH_{Ll}$ model, atomic displacement parameters for the whole model including waters were anisotropically refined. In the final rounds of refinement, hydrogen atoms in riding positions were added to this model using Reduce (84) as implemented in Phenix to improve the geometry. Finally, ordered solvent occupancies were refined. Figures of protein structures were

created using Pymol (Schrödinger LLC) (85). The $RelH_{Ll}$ dimer was reconstructed through the crystallographic symmetry operation across a two-fold crystallographic symmetry axis (Fig. S10).

SEC-MALS analysis

For each sample, 20 µl of purified protein at 5 mg/ml was injected on a Superdex 75 Increase 10/300 GL column (GE Healthcare) and MALS spectra recorded using inline DAWN-HELEOS light scattering and Optilab T-rEX refractive index detectors. Prior to the runs, a bovine serum albumin control was used to calibrate the instrument. The mass was determined by analyzing the differential refractive index using the Debye model for proteins (86) integrated in the ASTRA VI software.

Time course and inhibition hydrolysis experiments

Hydrolysis reactions were prepared in 50 mM Hepes, pH 8, 200 mM KCl, 1 mM $MnCl_2$ with pppGpp or ppGpp (Jena Bioscience) added to each test tube to a final concentration of 50 µM. Due to the large differences in hydrolysis rates, $RelH_{Cg}$ was added to a final concentration of 0.05 µM, while $RelH_{Ll}$ was at a concentration of 2.5 µM. The reactions were conducted at 30 °C in triplicate at 0, 2, 5, 15, 30, 60, 120, and, additionally for pppGpp, 180 min. At each time point, 100 µl of the reaction was removed and 5 mM EDTA added to quench the reaction. This sample was then injected into a 1 ml MonoQ 5/50 GL column (GE Healthcare) equilibrated in 50 mM Hepes, pH 8, 10 mM KCl. Separation of the substrates pppGpp and ppGpp from their respective products GTP and GDP was performed in a 50 mM Hepes, pH 8 buffer with a salt gradient ranging from 10 to 380 mM KCl. Product inhibition experiments were performed as above but in duplicates. Samples were incubated for 60 min with the addition of GTP or GDP to the reaction mix at concentrations of 0, 50, 100, 200, and 400 µM, before adding active enzyme. The concentration of remaining alarmone was determined based on the normalized (p)ppGpp peak area compared to time 0 controls, as calculated by the UNICORN evaluation software. Graphs were plotted using GraphPad Prism. Specific activity was calculated based on the initial rate of hydrolysis from time course measurements up to the 15-min mark, which produce a straight line.

DRaCALA binding and competition assays

DRaCALA binding and competition assays were performed essentially as previously described (49, 56). Briefly, purified $RelH_{Cg}$ or $RelH_{Ll}$ (at final concentrations of 100 µM) were incubated with 2 nM α-^{32}P-pppGpp or α-^{32}P-GTP in the presence of 100 µM cold competitor nucleotide, that is, GTP, GDP, pppGpp, or ppGpp. The binding solutions were incubated for 5 min at room temperature before 2 µl were spotted onto a nitrocellulose membrane. The fraction bound was quantified as described (56). Two biological replicates were performed, and the average and SD of the binding fractions were plotted *via* GraphPad Prism. One-way ANOVA and Dunnett's multiple comparison tests were performed to assess the presence of statistically significant differences.

AlphaFold2 prediction models

Full-length protein sequences of $RelH_{Cg}$, $RelH_{Ll}$, *Pa*SAH, $RelH_{Lm}$, $Mesh1_{Hs}$, and $Mesh1_{Dm}$ were used to create prediction models of homodimers using the AlphaFold2 pipeline (53) with the multimer procedure (62) *via* Colabfold (87). Multiple sequence alignment search was performed using the MMseq2 API (88).

Sequence alignments

Pairwise protein sequence alignment and multiple protein sequence alignment were performed using EMBOSS Needle and Clustal Omega, respectively (89). The structure-based sequence alignment was performed using PROMALS3D (90). All alignments were rendered with the aid of the ESPript 3.0 server (91).

Data availability

Atomic coordinates and structure factors of $RelH_{Cg}$ and $RelH_{Ll}$ structures presented in this article have been deposited at the RCSB Protein Data Bank (PDB) under the following identifiers: 7QOC (RelHCg, Se-Met form), 7QOD (RelHCg, native), and 7QOE (RelHLl, native).

Supporting information—This article contains supporting information (23, 41–43).

Acknowledgments—The authors would like to thank David von Stetten and Dmitry Molodenskiy for the assistance during data collection at beamlines P12, P13, and P14 operated by EMBL Hamburg at the PETRA III storage ring (DESY, Hamburg, Germany).

Author contributions—D. E. O., Y. E. Z., and D. E. B. conceptualization; D. E. O., Y. E. Z., and D. E. B. funding acquisition; D. E. O., Y. E. Z., and D. E. B. resources; F. B., D. E. O., Y. E. Z., and D. E. B. supervision; F. B., A. C., S.-D. Z., J. N. P., Y. E. Z., and D. E. B. investigation; F. B. and D. E. B. data curation; F. B., S.-D. Z., and Y. E. Z. methodology; F. B., A. C., Y. E. Z., and D. E. B. writing–original draft; D. E. O., Y. E. Z., and D. E. B. writing–review and editing.

Funding and additional information—This work was supported by a grant to D. E. B. (grant no. NNF18OC0030646), a grant to Y. E. Z. (grant no. NNF19OC0058331), and a grant to D. E. O. (grant no. NNF14OC0012953) from the Novo Nordisk Foundation.

Conflict of interest—The authors declare that they have no conflicts of interest with the contents of the article.

Abbreviations—The abbreviations used are: DRaCALA, differential radial capillary action of ligand assay; HD, hydrolase domain; PDB, protein data bank; pGpp, guanosine 3′-diphosphate 5′-monophosphate; ppGpp, guanosine 3′,5′-bis(diphosphate); pppGpp, guanosine 3′-diphosphate 5′-trisphosphate; RSH, RelA-SpoT homolog; SAH, small alarmone hydrolase; SAS, small alarmone

synthetase; Se-Met, seleno-methionine; TLS, translation-libration-screw-rotation.

References

1. Irving, S. E., Choudhury, N. R., and Corrigan, R. M. (2021) The stringent response and physiological roles of (pp)pGpp in bacteria. *Nat. Rev. Microbiol.* **19**, 256–271
2. Irving, S. E., and Corrigan, R. M. (2018) Triggering the stringent response: signals responsible for activating (p)ppGpp synthesis in bacteria. *Microbiology (Reading)* **164**, 268–276
3. Kriel, A., Bittner, A. N., Kim, S. H., Liu, K., Tehranchi, A. K., Zou, W. Y., *et al.* (2012) Direct regulation of GTP homeostasis by (p)ppGpp: a critical component of viability and stress resistance. *Mol. Cell* **48**, 231–241
4. Srivatsan, A., and Wang, J. D. (2008) Control of bacterial transcription, translation and replication by (p)ppGpp. *Curr. Opin. Microbiol.* **11**, 100–105
5. Ronneau, S., and Hallez, R. (2019) Make and break the alarmone: regulation of (p)ppGpp synthetase/hydrolase enzymes in bacteria. *FEMS Microbiol. Rev.* **43**, 389–400
6. Traxler, M. F., Summers, S. M., Nguyen, H. T., Zacharia, V. M., Hightower, G. A., Smith, J. T., *et al.* (2008) The global, ppGpp-mediated stringent response to amino acid starvation in Escherichia coli. *Mol. Microbiol.* **68**, 1128–1148
7. Primm, T. P., Andersen, S. J., Mizrahi, V., Avarbock, D., Rubin, H., and Barry, C. E. (2000) The stringent response of Mycobacterium tuberculosis is required for long-term survival. *J. Bacteriol.* **182**, 4889–4898
8. Weiss, L. A., and Stallings, C. L. (2013) Essential roles for Mycobacterium tuberculosis Rel beyond the production of (p)ppGpp. *J. Bacteriol.* **195**, 5629–5638
9. Kudrin, P., Varik, V., Oliveira, S. R. A., Beljantseva, J., Del Peso Santos, T., Dzhygyr, I., *et al.* (2017) Subinhibitory concentrations of bacteriostatic antibiotics induce relA-dependent and relA-independent tolerance to beta-lactams. *Antimicrob. Agents Chemother.* **61**, e02173-16
10. Abranches, J., Martinez, A. R., Kajfasz, J. K., Chávez, V., Garsin, D. A., and Lemos, J. A. (2009) The molecular alarmone (p)ppGpp mediates stress responses, vancomycin tolerance, and virulence in Enterococcus faecalis. *J. Bacteriol.* **191**, 2248–2256
11. Khakimova, M., Ahlgren, H. G., Harrison, J. J., English, A. M., and Nguyen, D. (2013) The stringent response controls catalases in Pseudomonas aeruginosa and is required for hydrogen peroxide and antibiotic tolerance. *J. Bacteriol.* **195**, 2011–2020
12. Potrykus, K., Murphy, H., Philippe, N., and Cashel, M. (2011) ppGpp is the major source of growth rate control in E. coli. *Environ. Microbiol.* **13**, 563–575
13. Potrykus, K., and Cashel, M. (2008) (p)ppGpp: still magical? *Annu. Rev. Microbiol.* **62**, 35–51
14. Artsimovitch, I., Patlan, V., Sekine, S.-I., Vassylyeva, M. N., Hosaka, T., Ochi, K., *et al.* (2004) Structural basis for transcription regulation by alarmone ppGpp. *Cell* **117**, 299–310
15. Cashel, M., and Gallant, J. (1969) Two compounds implicated in the function of the RC gene of Escherichia coli. *Nature* **221**, 838–841
16. Cashel, M., and Kalbacher, B. (1970) The control of ribonucleic acid synthesis in Escherichia coli: V. Characterization of a nucleotide associated with the stringent response. *J. Biol. Chem.* **245**, 2309–2318
17. Fung, D. K., Yang, J., Stevenson, D. M., Amador-Noguez, D., and Wang, J. D. (2020) Small alarmone synthetase SasA expression leads to concomitant accumulation of pGpp, ppApp, and AppppA in Bacillus subtilis. *Front. Microbiol.* **11**, 2083
18. Gaca, A. O., Kudrin, P., Colomer-Winter, C., Beljantseva, J., Liu, K., Anderson, B., *et al.* (2015) From (p)ppGpp to (pp)pGpp: characterization of regulatory effects of pGpp synthesized by the small alarmone synthetase of Enterococcus faecalis. *J. Bacteriol.* **197**, 2908–2919
19. Yang, J., Anderson, B. W., Turdiev, A., Turdiev, H., Stevenson, D. M., Amador-Noguez, D., *et al.* (2020) The nucleotide pGpp acts as a third alarmone in Bacillus, with functions distinct from those of (p) ppGpp. *Nat. Commun.* **11**, 5388
20. Atkinson, G. C., Tenson, T., and Hauryliuk, V. (2011) The RelA/SpoT homolog (RSH) superfamily: distribution and functional evolution of ppGpp synthetases and hydrolases across the tree of life. *PLoS One* **6**, e23479
21. Patil, P. R., Vithani, N., Singh, V., Kumar, A., and Prakash, B. (2020) A revised mechanism for (p)ppGpp synthesis by Rel proteins: the critical role of the 2'-OH of GTP. *J. Biol. Chem.* **295**, 12851–12867
22. Sy, J., and Lipmann, F. (1973) Identification of the synthesis of guanosine tetraphosphate (MS I) as insertion of a pyrophosphoryl group into the 3′-position in guanosine 5′-diphosphate. *Proc. Natl. Acad. Sci. U. S. A.* **70**, 306–309
23. Hogg, T., Mechold, U., Malke, H., Cashel, M., and Hilgenfeld, R. (2004) Conformational antagonism between opposing active sites in a bifunctional RelA/SpoT homolog modulates (p)ppGpp metabolism during the stringent response. *Cell* **117**, 57–68
24. Aravind, L., and Koonin, E. V. (1998) The HD domain defines a new superfamily of metal-dependent phosphohydrolases. *Trends Biochem. Sci.* **23**, 469–472
25. Mechold, U., Murphy, H., Brown, L., and Cashel, M. (2002) Intramolecular regulation of the opposing (p)ppGpp catalytic activities of Rel(Seq), the Rel/Spo enzyme from Streptococcus equisimilis. *J. Bacteriol.* **184**, 2878–2888
26. Arenz, S., Abdelshahid, M., Sohmen, D., Payoe, R., Starosta, A. L., Berninghausen, O., *et al.* (2016) The stringent factor RelA adopts an open conformation on the ribosome to stimulate ppGpp synthesis. *Nucleic Acids Res.* **44**, 6471–6481
27. Brown, A., Fernández, I. S., Gordiyenko, Y., and Ramakrishnan, V. (2016) Ribosome-dependent activation of stringent control. *Nature* **534**, 277–280
28. Loveland, A. B., Bah, E., Madireddy, R., Zhang, Y., Brilot, A. F., Grigorieff, N., *et al.* (2016) Ribosome*RelA structures reveal the mechanism of stringent response activation. *Elife* **5**, e17029
29. Takada, H., Roghanian, M., Caballero-Montes, J., Van Nerom, K., Jimmy, S., Kudrin, P., *et al.* (2021) Ribosome association primes the stringent factor Rel for tRNA-dependent locking in the A-site and activation of (p)ppGpp synthesis. *Nucleic Acids Res.* **49**, 444–457
30. Takada, H., Roghanian, M., Murina, V., Dzhygyr, I., Murayama, R., Akanuma, G., *et al.* (2020) The C-terminal RRM/ACT domain is crucial for fine-tuning the activation of 'long' RelA-SpoT homolog enzymes by ribosomal complexes. *Front. Microbiol.* **11**, 277
31. Tamman, H., Van Nerom, K., Takada, H., Vandenberk, N., Scholl, D., Polikanov, Y., *et al.* (2020) A nucleotide-switch mechanism mediates opposing catalytic activities of Rel enzymes. *Nat. Chem. Biol.* **16**, 834–840
32. Steinchen, W., and Bange, G. (2016) The magic dance of the alarmones (p)ppGpp. *Mol. Microbiol.* **101**, 531–544
33. Steinchen, W., Zegarra, V., and Bange, G. (2020) (p)ppGpp: magic modulators of bacterial physiology and metabolism. *Front. Microbiol.* **11**, 2072
34. Dalebroux, Z. D., Svensson, S. L., Gaynor, E. C., and Swanson, M. S. (2010) ppGpp conjures bacterial virulence. *Microbiol. Mol. Biol. Rev.* **74**, 171–199
35. Dalebroux, Z. D., and Swanson, M. S. (2012) ppGpp: magic beyond RNA polymerase. *Nat. Rev. Microbiol.* **10**, 203–212
36. Gaca, A. O., Colomer-Winter, C., and Lemos, J. A. (2015) Many means to a common end: the intricacies of (p)ppGpp metabolism and its control of bacterial homeostasis. *J. Bacteriol.* **197**, 1146–1156
37. Steinchen, W., Schuhmacher, J. S., Altegoer, F., Fage, C. D., Srinivasan, V., Linne, U., *et al.* (2015) Catalytic mechanism and allosteric regulation of an oligomeric (p)ppGpp synthetase by an alarmone. *Proc. Natl. Acad. Sci. U. S. A.* **112**, 13348–13353
38. Jimmy, S., Saha, C. K., Kurata, T., Stavropoulos, C., Oliveira, S. R. A., Koh, A., *et al.* (2020) A widespread toxin–antitoxin system exploiting growth control via alarmone signaling. *Proc. Natl. Acad. Sci. U. S. A.* **117**, 10500–10510
39. Kurata, T., Brodiazhenko, T., Alves Oliveira, S. R., Roghanian, M., Sakaguchi, Y., Turnbull, K. J., *et al.* (2021) RelA-SpoT homolog toxins pyrophosphorylate the CCA end of tRNA to inhibit protein synthesis. *Mol. Cell* **81**, 3160–3170.e9

40. Pausch, P., Abdelshahid, M., Steinchen, W., Schäfer, H., Gratani, F. L., Freibert, S.-A., *et al.* (2020) Structural basis for regulation of the opposing (p)ppGpp synthetase and hydrolase within the stringent response orchestrator Rel. *Cell Rep.* **32**, 108157
41. Singal, B., Balakrishna, A. M., Nartey, W., Manimekalai, M. S. S., Jeyakanthan, J., and Grüber, G. (2017) Crystallographic and solution structure of the N-terminal domain of the Rel protein from Mycobacterium tuberculosis. *FEBS Lett.* **591**, 2323–2337
42. Steinchen, W., Ahmad, S., Valentini, M., Eilers, K., Majkini, M., Altegoer, F., *et al.* (2021) Dual role of a (p)ppGpp- and (p)ppApp-degrading enzyme in biofilm formation and interbacterial antagonism. *Mol. Microbiol.* **115**, 1339–1356
43. Sun, D., Lee, G., Lee, J. H., Kim, H.-Y., Rhee, H.-W., Park, S.-Y., *et al.* (2010) A metazoan ortholog of SpoT hydrolyzes ppGpp and functions in starvation responses. *Nat. Struct. Mol. Biol.* **17**, 1188–1194
44. Ding, C.-K. C., Rose, J., Sun, T., Wu, J., Chen, P.-H., Lin, C.-C., *et al.* (2020) MESH1 is a cytosolic NADPH phosphatase that regulates ferroptosis. *Nat. Metab.* **2**, 270–277
45. He, H., Cooper, J. N., Mishra, A., and Raskin, D. M. (2012) Stringent response regulation of biofilm formation in Vibrio cholerae. *J. Bacteriol.* **194**, 2962–2972
46. McLennan, A. G. (2013) Substrate ambiguity among the nudix hydrolases: biologically significant, evolutionary remnant, or both? *Cell. Mol. Life Sci.* **70**, 373–385
47. Ito, D., Kato, T., Maruta, T., Tamoi, M., Yoshimura, K., and Shigeoka, S. (2012) Enzymatic and molecular characterization of Arabidopsis ppGpp pyrophosphohydrolase, AtNUDX26. *Biosci. Biotechnol. Biochem.* **76**, 2236–2241
48. Ooga, T., Ohashi, Y., Kuramitsu, S., Koyama, Y., Tomita, M., Soga, T., *et al.* (2009) Degradation of ppGpp by nudix pyrophosphatase modulates the transition of growth phase in the Bacterium Thermus thermophilus. *J. Biol. Chem.* **284**, 15549–15556
49. Zhang, Y., Zborníková, E., Rejman, D., Gerdes, K., and Swanson, M. S. (2018) Novel (p)ppGpp binding and metabolizing proteins of Escherichia coli. *mBio* **9**, e02188-17
50. Ruwe, M., Rückert, C., Kalinowski, J., and Persicke, M. (2018) Functional characterization of a small alarmone hydrolase in Corynebacterium glutamicum. *Front. Microbiol.* **9**, 1–16
51. Ruwe, M., Persicke, M., Busche, T., Müller, B., and Kalinowski, J. (2019) Physiology and transcriptional analysis of (p)ppGpp-related regulatory effects in Corynebacterium glutamicum. *Front. Microbiol.* **10**, 2769
52. Krissinel, E., and Henrick, K. (2007) Inference of macromolecular assemblies from crystalline state. *J. Mol. Biol.* **372**, 774–797
53. Jumper, J., Evans, R., Pritzel, A., Green, T., Figurnov, M., Ronneberger, O., *et al.* (2021) Highly accurate protein structure prediction with AlphaFold. *Nature* **596**, 583–589
54. Orr, M. W., and Lee, V. T. (2017) Differential radial capillary action of ligand assay (DRaCALA) for high-throughput detection of protein–metabolite interactions in bacteria. In: Nordenfelt, P., Collin, M., eds. *Bacterial Pathogenesis: Methods and Protocols*, Springer New York, New York, NY: 25–41
55. Roelofs, K. G., Wang, J., Sintim, H. O., and Lee, V. T. (2011) Differential radial capillary action of ligand assay for high-throughput detection of protein-metabolite interactions. *Proc. Natl. Acad. Sci. U. S. A.* **108**, 15528–15533
56. Schicketanz, M. L., Długosz, P., and Zhang, Y. E. (2021) Identifying the binding proteins of small ligands with the differential radial capillary action of ligand assay (DRaCALA). *J. Vis. Exp.* https://doi.org/10.3791/62331
57. Thornton, J. M., Laskowski, R. A., and Borkakoti, N. (2021) AlphaFold heralds a data-driven revolution in biology and medicine. *Nat. Med.* **27**, 1666–1669
58. Tunyasuvunakool, K., Adler, J., Wu, Z., Green, T., Zielinski, M., Žídek, A., *et al.* (2021) Highly accurate protein structure prediction for the human proteome. *Nature* **596**, 590–596
59. Varadi, M., Anyango, S., Deshpande, M., Nair, S., Natassia, C., Yordanova, G., *et al.* (2022) AlphaFold protein structure database: massively expanding the structural coverage of protein-sequence space with high-accuracy models. *Nucleic Acids Res.* **50**, D439–D444
60. David, A., Islam, S., Tankhilevich, E., and Sternberg, M. J. E. (2021) The AlphaFold database of protein structures: a biologist's guide. *J. Mol. Biol.* **434**, 167336
61. [preprint] Akdel, M., Pires, D. E. V., Porta Pardo, E., Jänes, J., Zalevsky, A. O., Mészáros, B., *et al.* (2021) A structural biology community assessment of AlphaFold 2 applications. *bioRxiv*. https://doi.org/10.1101/2021.09.26.461876
62. [preprint] Evans, R., O'Neill, M., Pritzel, A., Antropova, N., Senior, A., Green, T., *et al.* (2021) Protein complex prediction with AlphaFold-multimer. *bioRxiv*. https://doi.org/10.1101/2021.10.04.463034
63. Bershtein, S., Kleiner, D., and Mishmar, D. (2021) Predicting 3D protein structures in light of evolution. *Nat. Ecol. Evol.* **5**, 1195–1198
64. Manav, M. C., Beljantseva, J., Bojer, M. S., Tenson, T., Ingmer, H., Hauryliuk, V., *et al.* (2018) Structural basis for (p)ppGpp synthesis by the Staphylococcus aureus small alarmone synthetase RelP. *J. Biol. Chem.* **293**, 3254–3264
65. Kriel, A., Brinsmade, S. R., Tse, J. L., Tehranchi, A. K., Bittner, A. N., Sonenshein, A. L., *et al.* (2014) GTP dysregulation in Bacillus subtilis cells lacking (p)ppGpp results in phenotypic amino acid auxotrophy and failure to adapt to nutrient downshift and regulate biosynthesis genes. *J. Bacteriol.* **196**, 189–201
66. Fernández-Coll, L., and Cashel, M. (2020) Possible roles for basal levels of (p)ppGpp: growth efficiency vs. surviving stress. *Front. Microbiol.* **11**, 592718
67. Cianci, M., Bourenkov, G., Pompidor, G., Karpics, I., Kallio, J., Bento, I., *et al.* (2017) P13, the EMBL macromolecular crystallography beamline at the low-emittance PETRA III ring for high- and low-energy phasing with variable beam focusing. *J. Synchrotron Radiat.* **24**, 323–332
68. Franz, H., Leupold, O., Röhlsberger, R., Roth, S. V., Seeck, O. H., Spengler, J., *et al.* (2006) Technical report: PETRA III: DESY's new high Brilliance third generation synchrotron radiation source. *Synchrotron Radiat. News* **19**, 25–29
69. Kabsch, W. (2010) XDS. *Acta Crystallogr. D Biol. Crystallogr.* **66**, 125–132
70. Skubák, P., and Pannu, N. S. (2013) Automatic protein structure solution from weak X-ray data. *Nat. Commun.* **4**, 2777
71. Potterton, E., Briggs, P., Turkenburg, M., and Dodson, E. J. (2003) A graphical user interface to the CCP4 program suite. *Acta Crystallogr. D Biol. Crystallogr.* **59**, 1131–1137
72. Winn, M. D., Ballard, C. C., Cowtan, K. D., Dodson, E. J., Emsley, P., Evans, P. R., *et al.* (2011) Overview of the CCP4 suite and current developments. *Acta Crystallogr. D Biol. Crystallogr.* **67**, 235–242
73. McCoy, A. J., Grosse-Kunstleve, R. W., Adams, P. D., Winn, M. D., Storoni, L. C., and Read, R. J. (2007) Phaser crystallographic software. *J. Appl. Crystallogr.* **40**, 658–674
74. Afonine, P. V., Grosse-Kunstleve, R. W., Echols, N., Headd, J. J., Moriarty, N. W., Mustyakimov, M., *et al.* (2012) Towards automated crystallographic structure refinement with phenix.refine. *Acta Crystallogr. D Biol. Crystallogr.* **68**, 352–367
75. Adams, P. D., Afonine, P. V., Bunkoczi, G., Chen, V. B., Davis, I. W., Echols, N., *et al.* (2010) PHENIX: a comprehensive Python-based system for macromolecular structure solution. *Acta Crystallogr. D Biol. Crystallogr.* **66**, 213–221
76. Bricogne, G., Blanc, E., Brandl, M., Flensburg, C., Keller, P., Paciorek, W., *et al.* (2016) *BUSTER Version 2.10.3*, Global Phasing Ltd, Cambridge, United Kingdom
77. Smart, O. S., Womack, T. O., Flensburg, C., Keller, P., Paciorek, W., Sharff, A., *et al.* (2012) Exploiting structure similarity in refinement: automated NCS and target-structure restraints in BUSTER. *Acta Crystallogr. D Biol. Crystallogr.* **68**, 368–380
78. Emsley, P., Lohkamp, B., Scott, W. G., and Cowtan, K. D. (2010) Features and development of Coot. *Acta Crystallogr. D Biol. Crystallogr.* **66**, 486–501
79. Chen, V. B., Arendall, W. B., III, Headd, J. J., Keedy, D. A., Immormino, R. M., Kapral, G. J., *et al.* (2010) MolProbity: all-atom structure validation for macromolecular crystallography. *Acta Crystallogr. D Biol. Crystallogr.* **66**, 12–21

80. Echols, N., Grosse-Kunstleve, R. W., Afonine, P. V., Bunkoczi, G., Chen, V. B., Headd, J. J., *et al.* (2012) Graphical tools for macromolecular crystallography in PHENIX. *J. Appl. Crystallogr.* **45**, 581–586
81. Painter, J., and Merritt, E. A. (2006) Optimal description of a protein structure in terms of multiple groups undergoing TLS motion. *Acta Crystallogr. D Biol. Crystallogr.* **62**, 439–450
82. Painter, J., and Merritt, E. A. (2006) TLSMD web server for the generation of multi-group TLS models. *J. Appl. Crystallogr.* **39**, 109–111
83. Smart, O. S., Womack, T. O., Sharff, A., Flensburg, C., Keller, P., Paciorek, W., *et al.* (2011) *Grade, Version 1.2.19*. Global Phasing Ltd., Cambridge, United Kingdom
84. Word, J. M., Lovell, S. C., Richardson, J. S., and Richardson, D. C. (1999) Asparagine and glutamine: using hydrogen atom contacts in the choice of side-chain amide orientation. *J. Mol. Biol.* **285**, 1735–1747
85. Schrodinger, LLC. (2015) *The PyMOL Molecular Graphics System, Version 2.5*. Schrodinger, LLC, New York, NY
86. Edelman, J. (1992) The low-temperature heat capacity of solid proteins. *Biopolymers* **32**, 209–218
87. [preprint] Mirdita, M., Ovchinnikov, S., and Steinegger, M. (2021) ColabFold - making protein folding accessible to all. *bioRxiv*. https://doi.org/10.1101/2021.08.15.456425
88. Mirdita, M., Steinegger, M., and Söding, J. (2019) MMseqs2 desktop and local web server app for fast, interactive sequence searches. *Bioinformatics* **35**, 2856–2858
89. Madeira, F., Park, Y. M., Lee, J., Buso, N., Gur, T., Madhusoodanan, N., *et al.* (2019) The EMBL-EBI search and sequence analysis tools APIs in 2019. *Nucleic Acids Res.* **47**, W636–W641
90. Pei, J., Kim, B.-H., and Grishin, N. V. (2008) PROMALS3D: a tool for multiple protein sequence and structure alignments. *Nucleic Acids Res.* **36**, 2295–2300
91. Robert, X., and Gouet, P. (2014) Deciphering key features in protein structures with the new ENDscript server. *Nucleic Acids Res.* **42**, W320–W324